Planar Hall effect and anisotropic magnetoresistance in thin films of the chiral antiferromagnet Mn$_3$Sn

Vinay Sharma, Rajeev Nepal, and Ramesh C. Budhani[*]

Department of Physics, Morgan State University, Baltimore, Maryland 21251, USA

Antiferromagnetic Weyl semimetals with spin chirality offer excellent platforms to address the Berry phase physics, which manifests prominently in several of their electro-optical and electromagnetic responses including as a large anomalous Hall effect (AHE) and spin Hall conductivity. The Mn$_3$Sn and Mn$_3$Ge compounds, where the Mn spins arrange in a kagome lattice, are examples of this class of materials. Here, we report on measurements of magnetotransport in c-axis textured Mn$_3$Sn thin films grown on the [111] plane of single-crystal MgO by dc magnetron sputtering. At room temperature, these films display a weak uncompensated magnetic moment of $\approx 0.12\,\mu_B/\text{f.u.}$ in the basal plane and a longitudinal resistivity (ρ_{xx}) $\approx 3.8\,\mu\Omega\text{m}$, which matches well with the bulk value. A residual resistivity ratio [$\rho_{xx}(300K)/\rho_{xx}(2K)$] of ≈ 3.92 further indicates the high quality of the films. While at 300 K a weak AHE together with field-linear Hall resistivity (ρ_{xy}) is observed in magnetic fields (H) applied perpendicular to the kagome planes, the temperature (T) dependence of ρ_{xy} shows prominent signatures of three magnetic phases in the temperature regime of 2–300 K. The ρ_{xy} also derives a nontrivial topological contribution ($\rho_{\text{THE}} \sim 1\text{n}\Omega\text{m}$) in the spin-glass phase which appears at $T \leqslant 100$ K. The origin of the ρ_{THE} is attributed to spin textures which may appear in a frustrated chiral spin order. Our measurements of anisotropic magnetoresistance (AMR) and the planar Hall effect (PHE) over a wide H-T phase space reveal the hitherto unseen effects in the three magnetic phases of Mn$_3$Sn. While the AMR and PHE are negative in the inverse triangular spin phase ($250\,\text{K} \leqslant T \leqslant T_N$), the helical phase ($100 \leqslant T \leqslant 250\,\text{K}$) is devoid of anisotropic in-plane resistivity, and the spin-glass phase shows a sign reversal of AMR with the increasing magnetic field. The origin of this sign change in AMR/PHE is attributed to the emergence of topologically protected spin textures like skyrmions where the fictitious effective magnetic field is estimated to be ≈ 4.4 Tesla.

I. INTRODUCTION

Antiferromagnets (AFMs) are considered the next-generation spintronic materials over conventional ferromagnets (FMs) owing to their fast switching speed, zero stray fields, and stability against field-induced distortions of spin arrangements [1]. A particularly fascinating class of AFMs is presented by compounds that lack structural inversion symmetry and possess a noncollinear arrangement of spins. Such systems host topologically nontrivial spin textures such as skyrmions [1]. The Heusler compounds of the type Mn$_3$Z ($Z =$ Sn and Ge) stabilized in DO_{19} crystal symmetry are examples of such materials. These binary Heuslers present an excellent class of topological materials where electron correlations lead to a large anomalous Hall effect (AHE) [2], Nernst effect [3,4], terahertz-generated AHE [5], and other outstanding properties [5,6]. The large spin Hall conductivity and chirality of noncollinear coplanar magnetic structure also make these compounds attractive for spintronic applications [7–10].

Mn$_3$Sn is an AFM with the Mn spins arranged in a kagome-type inverse triangular structure stabilized due to geometric frustration and the Dzyaloshinskii-Moriya interaction [11]. The triangular 120° arrangement of Mn spins on the [0001] plane, set at the Néel temperature of 420 K, yields a net uncompensated in-plane magnetic moment of the order $\approx 20\,\text{m}\mu_B/\text{f.u.}$ at 300 K [2,3]. A weak interplanar spin interaction stabilizes a helical phase at ≈ 250 K which changes to a spin-glass state at $T < 100$ K [12]. For utilizing the full functionality of Mn$_3$Sn magnetic phases, epitaxial films of this compound have been synthesized on single-crystal substrates of Al$_2$O$_3$, SrTiO$_3$, MgO, and yttria stabilized zirconia [13–19]. The physical phenomenon that has been studied extensively in such films is the AHE [13–16]. However, a large AHE is observed only in films where the c axis of the hexagonal structure is on the plane of the substrate. The zero-field Hall resistivity is the least in epitaxial films with an out-of-substrate-plane c axis [14]. The large AHE and topological Hall effect (THE) in triangular AFMs have been explained by the Berry phase concept [20]. The origin of the THE is attributed to the breaking of time-reversal symmetry and evolution of real-space Berry curvature which gives rise to a nonzero topological winding of spin textures such as skyrmions [20]. The small size and topological aspects of skyrmions may enable the potential realization of ultrahigh-density nonvolatile memories [20,21]. However, the nontrivial topological spin textures and skyrmions are difficult to affirmatively identify using AHE measurements. Recently, Xu *et al.* [22] reported the presence of Néel skyrmions in

*Ramesh.budhani@morgan.edu

the Mn$_3$Sn/CoTb interface using advanced four-dimensional Lorentz scanning transmission electron microscopy, in combination with x-ray magnetic circular dichroism photoemission electron microscopy (XMCD-PEEM). Techniques like Lorentz microscopy, XMCD-XPEEM, and spin-polarized scanning tunneling microscopy have been used to image spin textures in chiral AFMs [20,23]. Interestingly, the measurements of anisotropic magnetoresistance (AMR) and the planar Hall effect (PHE) provide a simpler and powerful means to address skyrmion dynamics in electrically conducting systems [24–28]. Measurements of the PHE have been used by Yokouchi *et al.* [24] to probe the topological spin texture in epitaxial films of MnSi. Similar measurements have been used as well to address the dynamics of spin textures in systems like Gd$_2$PdSi$_3$ and Fe$_5$Sn$_3$ [25–28]. Although anisotropic magnetotransport (AMR/PHE) measurements have been conducted on single crystals of Mn$_3$Sn [3,29], these are limited to a small region of the *H-T* phase space. Moreover, studies of the temperature and magnetic field dependence of AMR/PHE and the signatures of skyrmion dynamics in such measurements in epitaxial films of Mn$_3$Sn are lacking.

In this paper, we present an extended study in *c*-axis textured Mn$_3$Sn thin films grown on the [111] surface of MgO. The temperature-dependent magnetotransport measurements in a Hall bar geometry reveal the appearance of three magnetic phases over a temperature regime of 2–300 K with their distinctive signatures in the AHE, AMR, and PHE. The exotic topological phase in the spin-glass state is also characterized by a sign reversal of AMR and the PHE with the increasing magnetic field and a topological contribution to the AHE.

II. EXPERIMENTAL DETAILS

Thin films with stack structure of [111] MgO/Mn$_3$Sn (100 nm)/Nb (2 nm) were deposited by dc magnetron sputtering of Mn$_{75}$Sn$_{25}$ (99.99%) and Nb (99.995%) targets in a load-lock multitarget high-vacuum system with a base pressure of 8×10^{-9} Torr. First, the MgO substrates were preheated to 700 °C for 20 min in high vacuum to remove any organic contaminants adsorbed on the surface. Since MgO is prone to adsorption of moisture, this heat treatment also allows removal of OH$^-$ radicals from its surface. After this step, the substrates were cooled to ambient temperature, and Mn$_3$Sn films were deposited at the rate of 0.07 nm/s in 5 mT of ultrahigh-purity (99.9999%) argon gas. The deposited films were annealed *in situ* at 500 °C for 20 min. Finally, a thin ($\approx$ 2-nm-thick) layer of niobium was deposited on top of the Mn$_3$Sn films at room temperature for protection against oxidation. The crystallographic structure and mosaicity of the films were measured with x-ray diffraction (XRD) using a Bruker D-8 Advance x-ray diffractometer with Cu$-K\alpha_1$ radiation. The Hall resistivity and AMR of these films were measured down to 2 K in a physical property measurement system equipped with a 9 Tesla superconducting magnet. Atomic force microscopy measurements were performed to image the surface topography of the films using an Asylum Research MFP-3D microscope.

III. RESULTS AND DISCUSSION

Mn$_3$Sn crystallizes in a hexagonal DO_{19}-type structure with space group $P63/mmc$ and lattice parameters $a = 5.665$ Å and $c = 4.531$ Å [2]. The Mn atoms are arranged in an inverse triangular manner forming the kagome layers stacked along the *c* axis, in which the Heisenberg interaction strength on up and down triangles is different, giving rise to a breathing anisotropy. The epitaxial relationship between [111] MgO and Mn$_3$Sn is illustrated in Figs. 1(a) and 1(b). Figure 1(c) shows the θ-2θ XRD pattern of a 100 nm Mn$_3$Sn thin film where the presence of [0002] and [0004] reflections of the hexagonal Mn$_3$Sn confirms that the [000n] reflections appear next to the cubic [111] reflections of MgO [31]. Mn$_3$Sn lattice constant *c* of 4.53 Å, determined from the [0002] reflection, is close to the bulk value [2]. The peaks near $2\theta = 41.8°$ and $42.2°$ in Fig. 1(d) are attributed to Mn$_2$Sn (11$\bar{2}$0) and Mn$_3$Sn (20$\bar{2}$1), respectively, arising presumably due to the Mn deficiency [15]. Figure 1(e) shows the full width at half maximum (FWHM) of a 100-nm-thick Mn$_3$Sn film. The FWHM $\approx 2°$, which establishes the level of mosaicity in the film. The surface roughness and topography of the film are analyzed using atomic force microscopy measurements, see Supplemental Material [32]. The Mn deficient samples show a helical magnetic phase transition ~ 250 K due to the formation of Mn$_2$Sn, which has a Curie temperature of ≈ 250 K [34]. The significance of this transition will be addressed further in the following sections.

Figure 2 shows the room-temperature magnetization loops of a Mn$_3$Sn film measured using a vibrating sample magnetometer. These data have been corrected for the diamagnetic response of the MgO substrate. The sample shows a weak FM response with a saturation moment of $\approx 0.12 \, \mu_B/$f.u. for the in-plane field. For the out-of-plane field, the moment drops to $\approx 0.08 \, \mu_B/$f.u. The weak moment seen for the in-plane field indicates a small canting of the Mn spins in the *a-b* plane, whereas the minuscule moment in the out-of-plane direction suggests some canting along the *c* axis as well. The small in-plane and out-of-plane moments seen here are an order of magnitude higher than the reported values for Mn$_3$Sn crystals ($4-7 \, m\mu_B/$f.u.) [2]. This discrepancy has been discussed previously in the context of disorder and Mn deficiency in thin films, which in turn generate the out-of-plane tilting of Mn moments [13,35]. The in-plane uncompensated moment in these epitaxial Mn$_3$Sn films was found to be $\sim 0.21 \, \mu_B/$f.u., which is approximately double the moment found in the present case. In these reports [13,35], the larger magnetization is attributed to the uncompensated moments arising due to the disorder and defects caused by excess of Sn atoms randomly occupying Mn sites as well as Mn vacancies [13]. We therefore argue that the Mn$_3$Sn films in the present case possess lower disorder and antisite defects. We also note an anisotropy in the coercive field (H_c) of these films, as shown in the inset of Fig. 2. The coercive field when the field is orientation along the [2$\bar{1}$10] direction ($\mu_0 H_c \approx 10$ mT) is higher by a factor of ≈ 3, as compared with H_c for the field orientation along [0001]. This is presumably due to the mosaicity of epitaxy in the *a-b* plane of the film, and the measured magnetization reflects an average over many crystallites [14].
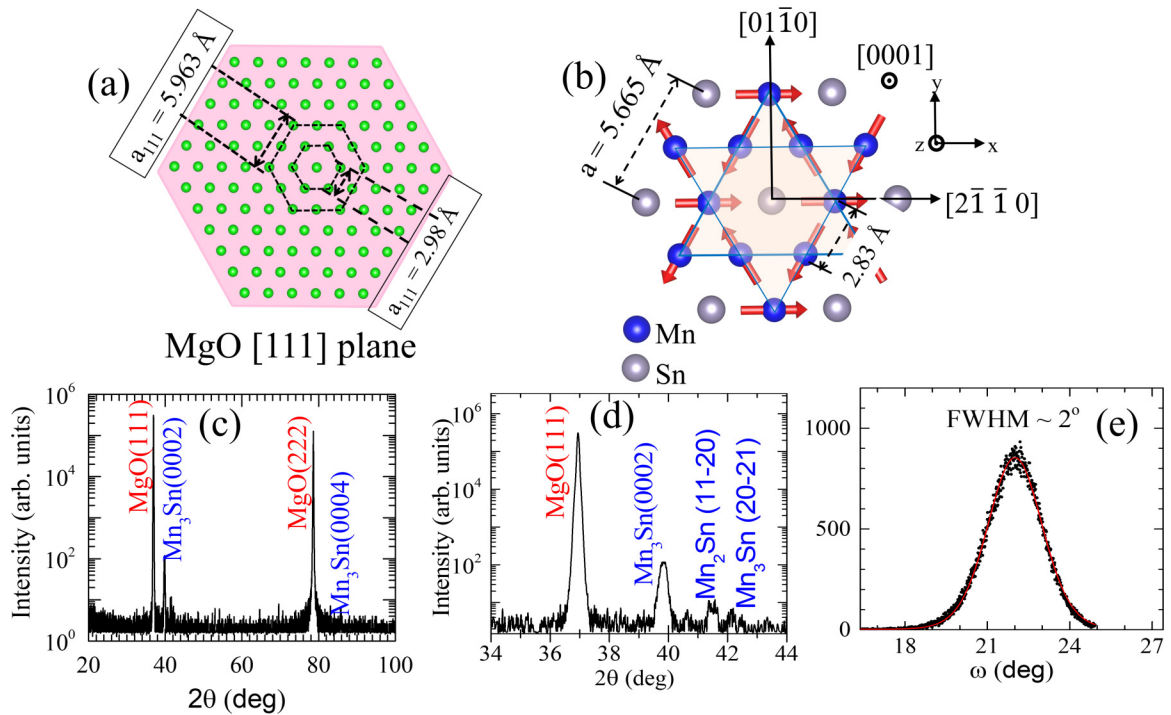
FIG. 1. (a) A sketch of atomic (Mg) positions on the $< 111 >$ plane of MgO, the Mg atoms are shown as green circles which form a hexagonal plane of lattice spacing 5.963 Å. (b) Atomic positions on the c plane of the Mn_3Sn lattice with in-plane ([$01\bar{1}0$], [$2\bar{1}\bar{1}0$]) and out-of-plane ([0001]) directions marked. The orientations of Mn spins are shown in the kagome plane. Crystal structures are drawn using VESTA software [30]. (c) θ-2θ x-ray diffraction (XRD) pattern of a 100-nm-thick Mn_3Sn film grown on MgO [111] substrate. c-plane crystallographic directions are marked. (d) shows the zoomed XRD near the (0002) peak where the small peaks $\sim 41.8°$ and $42.2°$ correspond to Mn_2Sn (11$\bar{2}$0) and Mn_3Sn (20$\bar{2}$1), respectively. (e) shows the rocking curve measurement near (0002) which gives the full width at half maximum value of $\sim 2°$.

The temperature-dependent magnetotransport measurements offer a powerful means to probe magnetic phase transitions in Mn_3Sn thin films. Here, we measure the
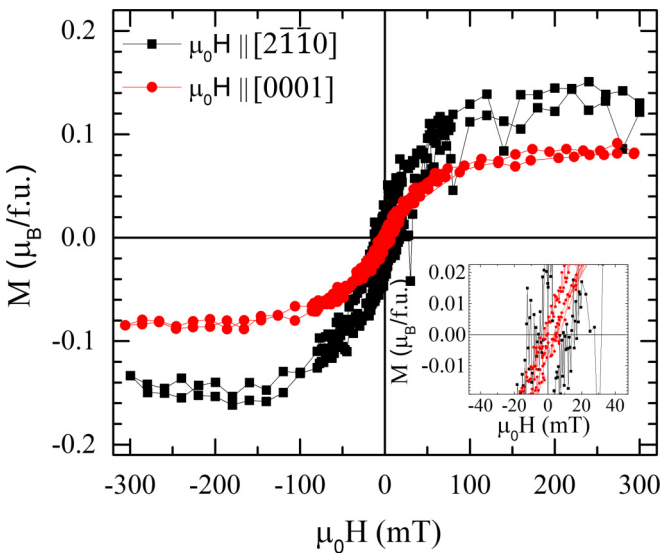

FIG. 2. Magnetization of a 100-nm-thick Mn_3Sn film at two orientations of the external field; in-plane parallel to ([$2\bar{1}\bar{1}0$]) and out-of-plane parallel to ([0001]) directions. Inset shows a magnified view of data near zero field to differentiate the coercive field in the in-plane and out-of-plane directions.

longitudinal (ρ_{xx}) and Hall (ρ_{xy}) resistivity of a 100-nm-thick Mn_3Sn film patterned in a Hall bar geometry, as shown in Fig. 3(a). The value of ρ_{xx} is extracted after symmetrizing the $+H$ and $-H$ data, i.e., $\rho_{xx} = [\rho_{xx}(+H) + \rho_{xx}(-H)]/2$, whereas the true ρ_{xy} is obtained on antisymmetrization of the transverse resistivities, i.e., $\rho_{xy} = [\rho_{xy}(+H) - \rho_{xy}(-H)]/2$. Figure 3(b) shows the ρ_{xx} (T) data, which confirms the metallic nature of Mn_3Sn as reported in works on bulk crystals [2]. The room-temperature ρ_{xx} of 3.8 $\mu\Omega$ m is close to the reported value (3.1 $\mu\Omega$ m) in epitaxial thin films [14]. The residual resistivity ratio (RRR ~ 3.92) marked in Fig. 3(b) is higher by a factor of ≈ 3 as compared with the result of Taylor *et al.* [14], suggesting a better-quality film. Figure 3(b) also shows that the ρ_{xx} curves measured at different magnetic fields overlap, indicating a very low ($\approx 0.1 - 0.3\%$) magnetoresistance (MR) for the out-of-film-plane-oriented magnetic field. This value is comparable with the previously measured MR in the out-of-plane field [14] and indicates the presence of weak magnetization in these AFM films.

The noncollinear AFMs like Mn_3Sn are known to display a giant AHE which could be used to identify different magnetic phase transitions in the material [3]. We have measured the ρ_{xy} of the Mn_3Sn films over a broad range of temperature and magnetic field strengths. Figure 3(c) shows the temperature-dependent ρ_{xy} measured with the magnetic field applied along the [0001] direction (perpendicular film plane). These data reveal two critical temperatures where ρ_{xy} undergoes a dramatic change. First, a well-defined cusp develops at $T \approx 250$ K,
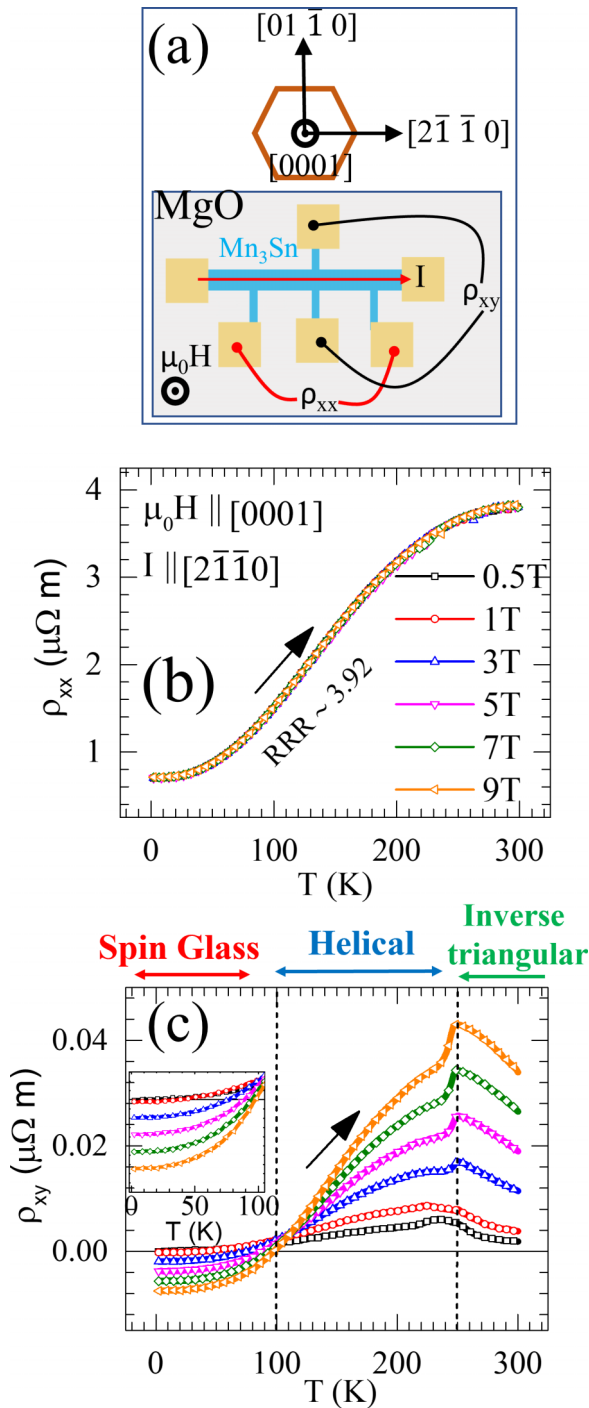
FIG. 3. (a) Schematic representation of magnetotransport measurements in a Hall bar geometry. (b) Longitudinal resistivity (ρ_{xx}) measured as a function of temperature at several values of magnetic field applied perpendicular to the plane of the film ($<0001>$) during field warming. (c) Hall resistivity (ρ_{xy}) measured as a function of temperature at different values of the out-of-plane magnetic field. The Hall resistivity clearly shows transitions from spin glass to helical and from helical order to inverse triangular antiferromagnetic order on warming from 2 to 300 K. These transitions are marked by dotted vertical lines. Inset shows a magnified view of the Hall data at $T < 100$ K.

which agrees well with the reported temperature of a magnetic transition from the inverse triangular spin structure to a helical phase on cooling below ambient temperature. The sharp drop in ρ_{xy} at this temperature may be related to a change in the mechanism of scattering or a change in the Berry curvature of electronic states at the Fermi energy. The second critical behavior of ρ_{xy} emerges at $T \approx 100$ K, where the system enters in a spin-glass state on cooling [36,37]. The ρ_{xy} below this critical point undergoes a sign change, which is evident in the magnified plot of the data at $T < 100$ K, shown in the inset of Fig. 3(c). While a giant zero-field AHE is seen in Mn_3Sn crystals when measured with the field in the *a-b* plane as a result of the noncollinearity of spins in the kagome planes [2,14], the out-of-*a-b*-plane field data presented in Fig. 3(c) are suggestive of spin canting along the *c* axis in the presence of a strong field [14]. We tentatively attribute the change in sign of ρ_{xy} below ≈ 100 K to the emergence of spin textures in the spin-glass phase which may contribute to a THE that counteracts the spin-canting contribution to $\rho_{xy} > 100$ K. We discuss this feature of ρ_{xy} in the next section.

We now present the measurements of Hall resistivity as a function of applied magnetic field at several temperatures to address its hysteretic behavior and its value at zero field. While the former is important to establish the orientational dynamics of Mn moments, the latter is related to the momentum space fictitious field seen by the conduction electrons. Figure 4(a) shows the variation of ρ_{xy} as a function of the out-of-plane magnetic field when current (I) is applied parallel to the [$2\bar{1}\bar{1}0$] direction. A linear Hall response ($d\rho_{xy}/dH = $ const.) is observed at 300 K. This linearity is primarily due to the ordinary Hall effect ($R_0\mu_0H$) because the weak magnetization of Mn_3Sn lies along the basal plane (*a-b* plane) which is orthogonal to the applied field direction. The carrier density obtained from this linear Hall response using the Drude relation is $\approx 1.7 \times 10^{21}$ cm^{-3}. In the temperature window of 250–100 K, we see a clear nonlinear Hall response in field $\mu_0H \leqslant 1$ Tesla. The linear extrapolations of the high-field ρ_{xy} ($\pm\mu_0H$) data to zero field and antisymmetrization of these zero-field values yield a zero-field AHE, which peaks to ≈ 5 nΩ m at 200 K. It is instructive to compare this number with the value of zero-field ρ_{xy} in polycrystalline and [0001]-oriented epitaxial films of Mn_3Sn. Authors of a previous report on epitaxial thin films have shown a very low value of ρ_{AHE} ($\rho_{AHE} < 1$ nΩ m) in the *c* plane and significantly higher value ($\rho_{AHE} > 2$ nΩ m) in *a-b*-plane-oriented samples [14]. In polycrystalline Mn_3Sn thin films, negative AHE is observed with a large coercivity [38].

A strikingly different Hall response is seen at $T \leqslant 100$ K. The zero-field ρ_{xy} is now very small, and at higher fields, it is linear with a negative slope. However, the zero-field value of ρ_{xy} remains positive albeit very small, as shown in the inset of Fig. 4(b). Since Mn_3Sn is known to transit to a spin-glass phase at $T < 100$ K, the frustrated Mn moments in this temperature regime may form topologically nontrivial spin textures which may lead to a topological contribution to ρ_{xy}. Consequently, the net Hall resistivity of our chiral magnet

FIG. 5. Sketch of longitudinal (ρ_{xx}) and transverse (ρ_{xy}) resistivity measurements as a function of angle (Φ). Here, current I flows along $[2\bar{1}\bar{1}0]$, and the magnetic field is applied in the a-b plane. ρ_{xx} and ρ_{xy} are measured along $[2\bar{1}\bar{1}0]$ and $[01\bar{1}0]$ directions, respectively. Corresponding electric fields E_{xx} and E_{xy} are also shown in this figure.

contributions from scattering and band structure effects such as anomalous velocity and Berry curvature [40]. The last term in Eq. (1) is the topological Hall resistivity (ρ_{THE}). The value of ρ_{THE} is calculated after subtracting the contributions of the ordinary Hall effect and AHE from the measured ρ_{xy}. In Fig. 4(b), we show ρ_{THE} at $T < 100$ K as a function of the out-of-plane magnetic field. To find ρ_{THE}, we first calculate the ordinary Hall contribution from the slope of the field linear Hall data. The AHE contribution is calculated by extrapolating the linear response to the zero field. The value of ρ_{THE} (H) is then extracted by subtracting the two contributions from measured ρ_{xy} (H), see Supplemental Material [32]. Figure 4(c) shows the relation between AHE resistivity and longitudinal resistivity to justify the standard scaling law of the good metal regime. The relation $\rho_{xy} \approx \rho_{xx}^{\alpha}$, with $\alpha = 1$, suggests that the AHE in Mn$_3$Sn is governed by the induced Berry curvature [40].

Electronic band structure calculations show that Mn$_3$Sn is a magnetic Weyl semimetal [41]. Together with the observation of a large zero-field anomalous Hall resistivity, the presence of a strong anisotropic backscattering of charge carriers in this material is an indicator of a time-reversal symmetry-broken Weyl semimetal. Here, we report on the behavior of temperature and magnetic field-dependent AMR and the PHE in Mn$_3$Sn epitaxial films whose Hall and out-of-plane MR data are reported in the earlier section.

Unlike the AHE, AMR and the PHE are even magnetotransport effects and thus symmetric under magnetic field reversal. Figure 5 shows a schematic of the AMR/PHE measurement geometry where current and magnetic field are applied in the plane of the film, while it is given an in-plane rotation of 360°. This allows a continuous variation of the angle Φ between the current and the magnetic field.

In a typical 3d FM like permalloy, the ϕ dependence of ρ_{xx} and ρ_{xy} for the in-plane field is expressed as [42–44]

$$\rho_{xx}(\Phi) = \rho_{\perp} + (\rho_{\|} - \rho_{\perp})\cos^2(\Phi), \tag{2}$$

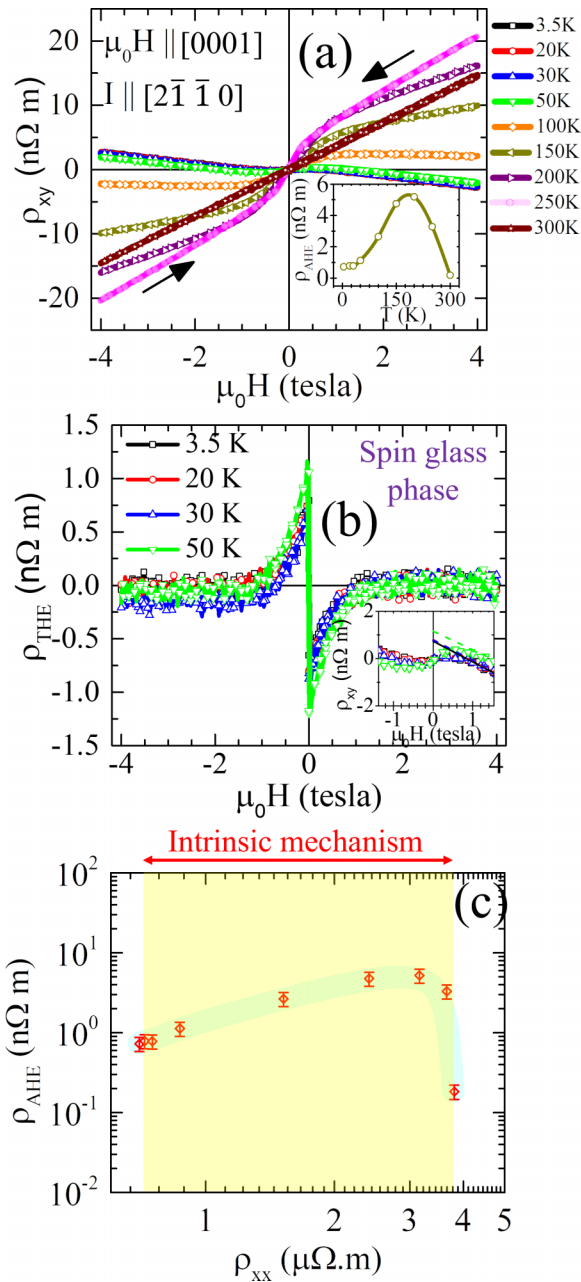$$\rho_{xy}(\Phi) = (\rho_{\|} - \rho_{\perp})\cos(\Phi)\sin(\Phi), \tag{3}$$

FIG. 4. (a) Hall resistivity at several temperatures plotted as a function of magnetic field applied parallel (//) to the film normal (// c axis) with current flow along the $[01\bar{1}0]$ direction. Inset shows the Hall resistivity derived from the anomalous Hall effect (AHE) contribution (ρ_{AHE}) which is calculated by the linear fitting at high field and extrapolated to the zero-field value. (b) Derived topological Hall effect in the spin-glass phase ($T < 100$ K). The inset of (b) shows the zero-field extrapolation of the Hall data to extract the topological contribution (see text). (c) Scaling relation between ρ_{AHE} and ρ_{xx} at different temperatures shows that Mn$_3$Sn sits in a good metal regime where the AHE generates due to intrinsic mechanism.

at $T < 100$ K may be expressed as [39]

$$\rho_{xy} = R_0\mu_0 H + \rho_{AHE} + \rho_{THE}, \tag{1}$$

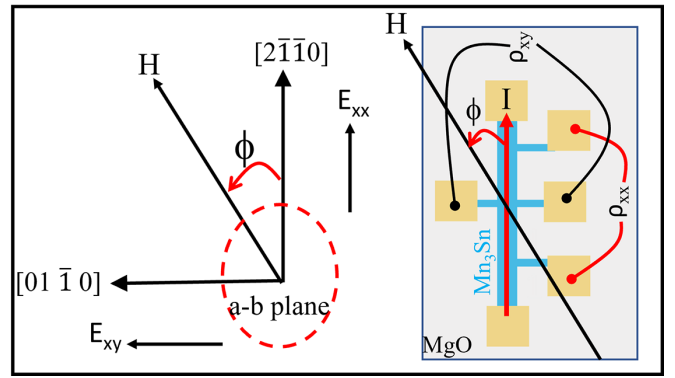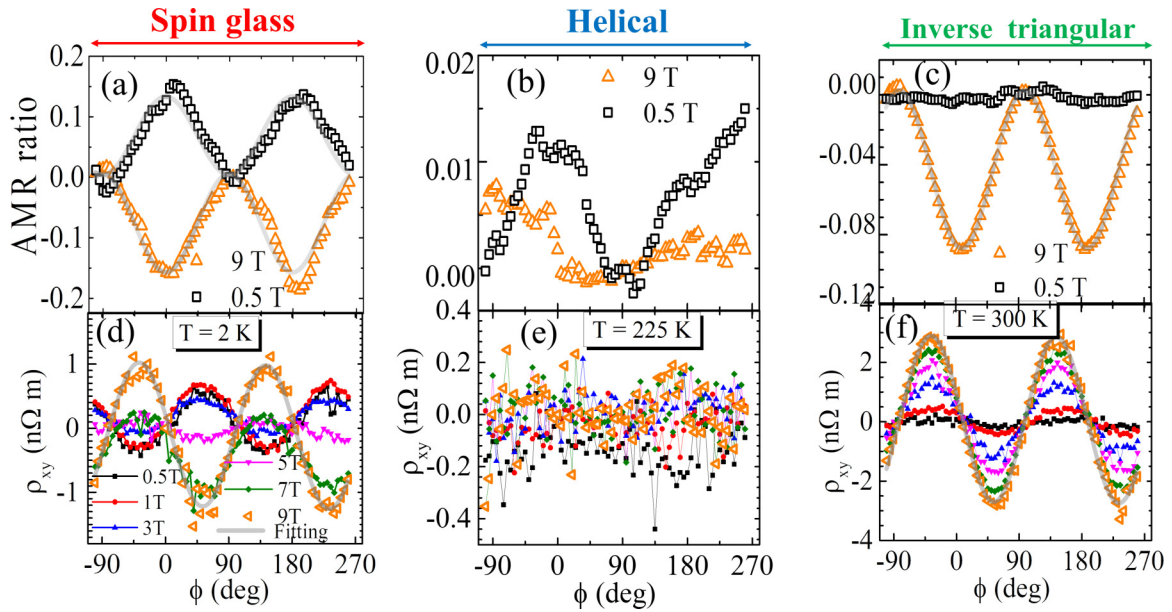where the first term accounts for the ordinary Hall effect, and the second term is the anomalous Hall which derives

FIG. 6. (a)–(c) Anisotropic magnetoresistance (AMR) ratio (= $\{[\rho_{xx}(\phi) - \rho_{xx}(\perp)/\rho_{xx}(\perp)\} \times 100$) as a function of angle Φ measured in three different magnetic phases ($T < 100$ K, 100 K $< T < 250$ K, and $T > 250$ K) of Mn_3Sn at lower (0.5 T) and higher (9 T) magnetic fields. (d)–(f) Transverse resistivity (ρ_{xy}) as a function of angle Φ measured in the temperature regimes $T < 100$ K, 100 K $< T < 250$ K, and $T > 250$ K corresponding to the spin glass, helical, and inverse triangular phases, respectively.

and the difference ($\rho_{||} - \rho_{\perp}$) defines ρ_{AMR}. The physical origin of AMR has been attributed to anisotropic *s-d* backscattering of conduction electrons due to high spin-orbit coupling of $3d$ orbitals [42,43]. This leads to a difference in the resistivity ($\rho_{||}$) when the current (I) and magnetization (M) are parallel and the resistivity ($\rho_{\perp}$) when I and M are orthogonal. While the difference ($\rho_{||} - \rho_{\perp}$) is generally positive in $3d$ FMs, this may not be the case in topological insulators and Weyl semimetals due to their special band topology, which leads to an interband contribution to conductivity and a nonzero Berry curvature of states near the Fermi energy which may be connected to chiral anomaly in transport [42].

We have measured the Φ dependence of ρ_{xx} and the PHE of Mn_3Sn films. Figure 6(a) shows the variation of the AMR ratio (= $\{[\rho_{xx}(\phi) - \rho_{xx}(\perp)]/\rho_{xx}(\perp)\} \times 100$) at 0.5 and 9.0 Tesla as a function of angle Φ measured at 2 K, where Mn_3Sn is in the spin-glass phase. Here, we emphasize that these data have been obtained after symmetrizing the measurements performed at the negative and positive field orientations to eliminate any contribution of anomalous Hall voltage that might creep in due to a misalignment between the magnetic field and the plane of the sample. While these data broadly follow the angular dependence predicted by Eq. (2), a sign reversal of AMR with increase in magnetic field at $T < 100$ K suggests a magnetic-field-induced change in charge career scattering. This field-induced change in sign of ($\rho_{||} - \rho_{\perp}$) is also seen in the ρ_{xy} data of the spin-glass phase [see Fig. 6(d)].

In Figs. 6(b) and 6(e), we show the angular dependence of the AMR ratio and ρ_{xy} at 225 K. Barring a small variation in ρ_{xx} at 0.5 Tesla, which is not in agreement with Eq. (2), the AMR and PHE display no angular dependence in the helical phase. This observation seems to suggest that the anisotropic backscattering here is directly related with the magnetization,

which is close to zero in the helical phase [2]. The AMR reappears along with the PHE when the sample temperature is raised above 250 K, where it is in the inverse triangular phase, as seen in Figs. 6(c) and 6(f), respectively. However, unlike the case of the spin-glass state, the AMR and PHE remain negative over the entire field range. Figures 7(a) and 7(b) summarize the behavior of ρ_{AMR} and ρ_{PHE} as a function of magnetic field in the three magnetic phases. In the spin-glass phase ($T = 2$ K), the sign change in AMR and the PHE from positive to negative occurs on increasing the field beyond ≈ 4 Tesla. We have analyzed the field dependence of the AMR and PHE measured at 300 K in the framework of a second-order polynomial and a quadratic function of magnetic field. A positive AMR with quadratic field dependence is generally seen in itinerant FMs due to the classical anisotropic orbital MR [45]. The data of Figs. 7(a) and 7(b) clearly deviate from this behavior and show a combination of linear and quadratic dependencies with negative overall values which may be attributed to chiral anomaly in the Weyl state. This type of higher-order harmonics in AMR/PHE can be a signature of Weyl fermions in Mn_3Sn, as previously reported in kagome-type AFMs [45]. The sign change in the 2 K data presumably reflects a crossover from the classical regime to the chirality-dominated transport.

The magnetic phases of Mn_3Sn are emphasized better by the temperature dependence of PHE measured at 0.5 and 9.0 Tesla, as shown in Fig. 8. The PHE and AMR are absent in the helical phase at all fields. The spin reorientation points at 250 and 100 K match well with the reported neutron diffraction studies [36]. The PHE signal is mainly dependent on the magnetic moment which is a continuously increasing function of applied magnetic field due to the noncollinear AFM nature of Mn_3Sn. At $T > 250$ K, Mn_3Sn magnetic moments lie in the *a-b* plane forming a coplanar inverse trian-
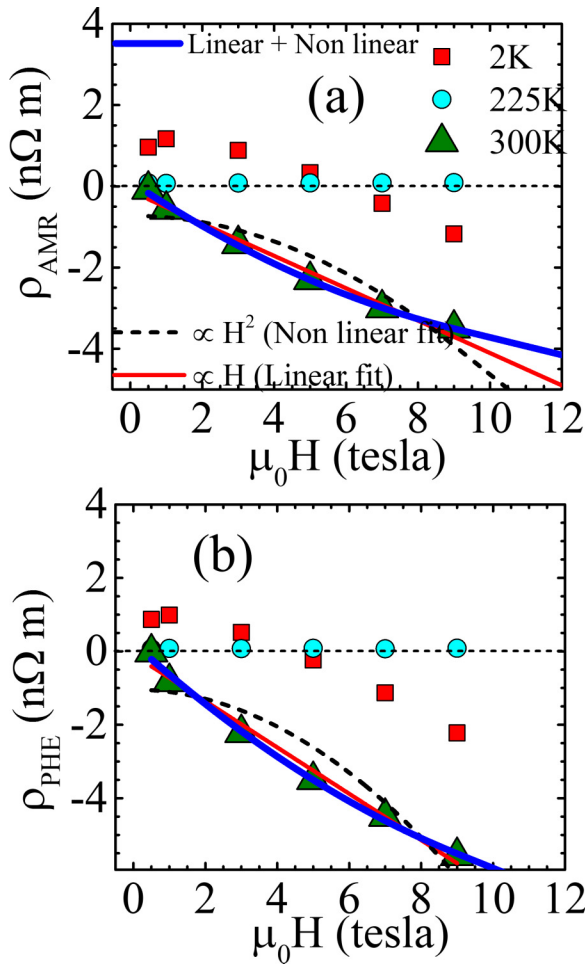
FIG. 7. (a) The calculated anisotropic magnetoresistance (AMR) as a function of magnetic field in the three magnetic phases. (b) Derived planar Hall resistivity as a function of magnetic field in three different magnetic phases of the film. The data taken in the inverse triangular phase ($T > 250$ K) have been fitted to a particular type of H dependence. Solid blue line and red line fitting corresponds to linear and second-order polynomial relation, while broken black line corresponds to quadratic (H^2) fitting. The H^2 dependence corresponds to the $3d$ ferromagnets, while the combination of linear and quadratic fitting is the signature of chiral anomaly.

gular orientation. This temperature-dependent PHE behavior mimics the field-cooled magnetization behavior of Mn_3Sn up to 100 K [12,46]. However, the increment in the PHE and the peculiar sign change at low temperature ($T < 100$ K) shown in Fig. 8 cannot be understood only by the temperature-dependent magnetization data of Mn_3Sn. We have done a detailed study of the temperature-dependent PHE in this range to shine light on this unexplored region.

A sign change in AMR/PHE driven by temperature and magnetic field has been observed earlier in various systems [42]. The sign-reversal phenomenon in very thin films (~4 nm) of hole-doped manganites on changing the magnetic field has been attributed to a change in magnetic anisotropy as the state of strain in the field changes with thickness [47]. A temperature-dependent sign change in AMR/PHE has also been observed in topological insulators [48]. Similar effects in AMR/PHE are seen as well in various Dirac and
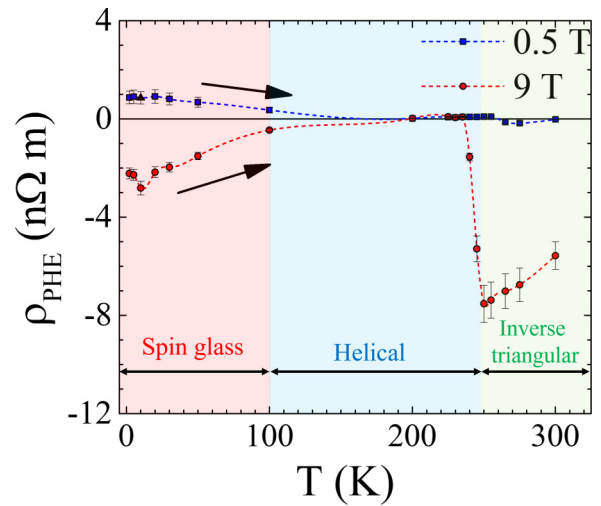

FIG. 8. Temperature-dependent planar Hall effect (PHE) resistivity calculated by fitting the $\rho_{xy}(\phi)$ data taken at 0.5 and 9.0 Tesla in-plane field to Eq. (3). All three magnetic phases of Mn_3Sn are revealed clearly by the PHE data. The square and circular data points are measured values, and dotted lines are guides to the eye.

Weyl semimetals where the chiral charge pumping and spin-flip backscattering break the time-reversal symmetry [42]. However, no similar effects have been reported in Mn_3Sn thin films.

We now address the sign reversal of PHE in the spin-glass phase in greater detail. Figure 9 shows the field dependence of the PHE at $T \leqslant 50$ K at several temperatures. These measurements are performed in such a manner that the sample is first demagnetized by an oscillating magnetic field to remove any residual magnetization and then the field of positive and negative polarity is applied to collect the ρ_{xy} (ϕ) data, as depicted in Fig. 5. The PHE remains positive if the magnetic field is less than ≈4.5 Tesla. At $H > 4.5$ Tesla, its sign reverses. This crossover point remains the same (≈ 4.5 Tesla) at all temperatures below ≈ 50 K. Authors of previous low-temperature neutron diffraction studies have identified a
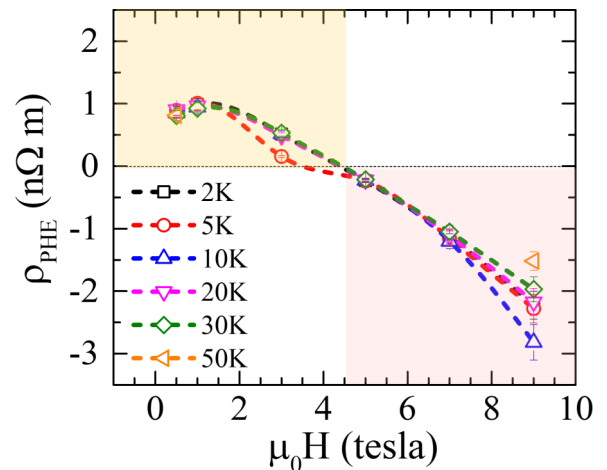

FIG. 9. Magnetic field dependence of the planar Hall effect (PHE) at several temperatures in the spin-glass state of Mn_3Sn. The broken lines in the figure are guides to the eye.

spin-glass phase in Mn_3Sn characterized by a slight random tilting of Mn moments away from the c plane [49]. Two possible scenarios have been presented for the canting on Mn moments: (i) all three magnetic moments of the inverse triangular structure tilt toward the positive c axis, and (ii) one moment tilts downward, and the other two tilt upward from the c plane. The second scenario is presumed to lead to the nontrivial topological spin textures and consequently the THE [20]. The strength of the THE in these Mn_3Sn films at $T \leqslant 50$ K has been presented earlier in Fig. 4(b). This observation of the THE in Mn_3Sn is also consistent with previous reports on noncoplanar magnetic systems like MnSi, Gd_2PdSi_3, and FeSb where the low-temperature topological spin textures have been attributed to the skyrmionic state [20,50,51].

We now address the sign change of the PHE in the spin-glass state of Mn_3Sn at a field of ≈ 4.5 Tesla in the framework of topological spin textures by expressing ρ_{THE} as [20,50]

$$\rho_{THE} = PR_0\mu_0H_{eff}, \quad (4)$$

where P is the local spin polarization of conduction electrons, R_0 is the normal Hall coefficient, and H_{eff} is the fictitious effective field arising from the Berry phase which orients opposite to the applied field [20]. We may now compare the value of the magnetic field at which the PHE changes sign (Fig. 9) with the calculated value of H_{eff}. For Mn_3Sn thin film, $\rho_{THE} \approx 1 n\Omega m$ [calculated from Fig. 4(b)], the value of R_0 calculated from Fig. 4(a) is $\approx 8.5 \times 10^{-10}$ Ω m/Tesla, and P is defined as the ratio of ordered magnetic moments in the spin-glass phase to the saturated magnetic moments and taken as $P \approx 0.27$ which is in a good agreement with the previously calculated values [11]. After putting all these values into Eq. (4), the fictitious effective field $\mu_0H_{eff} \approx 4.4$ Tesla, which is in remarkable agreement with the experimental value obtained in Fig. 9. Hence, we may argue that the nontrivial topological spin texture and the PHE sign change in the spin-glass phase are closely related. We also speculate that the growth of $\rho_\perp$ with field above a critical field (≈ 4.4 Tesla) is smaller than the growth of $\rho_{||}$. This is likely to happen when the orbit of conduction electrons in the configuration where magnetic field perpendicular to the direction of current ($\mathbf{J}\perp\mathbf{B}$) becomes smaller on increasing the field. This may lead to a suppression of charge carrier scattering by magnetic textures and surfaces and hence a weakened growth of $\rho_\perp$ with field. The disappearance of the THE above a critical field also suggests that the carrier scattering by the spin textures like skyrmions in the $\mathbf{J}\perp\mathbf{B}$ geometry disappears altogether above the critical field. Further exploration of this fictitious magnetic field and skyrmions in Mn_3Sn are suitable subjects for future studies.

IV. SUMMARY AND CONCLUSIONS

In summary, we have conducted detailed measurements of anisotropic in-plane magnetotransport and the AHE in c-axis-oriented thin films of chiral AFM Mn_3Sn over a wide H-T phase space. These films were deposited on the [111] surface of MgO crystals using ultrahigh vacuum magnetron sputtering. The magnetic hysteresis loops of the films measured at 300 K reveal a weak magnetic moment arising due to the canting of Mn spins toward the c axis. We have established the presence of three distinct magnetic phases in this chiral magnet through the measurements of the AHE, AMR, and PHE over a temperature range of 2–300 K. While the helical phase stabilized between ≈ 100 and 250 K is devoid of anisotropic in-plane transport, the spin-glass phase formed at $T < 100$ K is characterized by a magnetic-field-dependent sign reversal of AMR and the PHE and a topological contribution to the Hall voltage which presumably comes from the nontrivial spin textures of the spin-glass phase. Notably, no such sign change of AMR/PHE is seen in the inverse triangular spin state of the system which occurs above ≈ 250 K. Direct imaging of the spin textures with Lorentz transmission electron microscopy in the spin-glass phase would be a highly desirable direction for further studies.

ACKNOWLEDGMENTS

[1] V. Baltz, A. Manchon, M. Tsoi, T. Moriyama, T. Ono, and Y. Tserkovnyak, Antiferromagnetic spintronics, Rev. Mod. Phys. **90**, 015005 (2018).

[2] S. Nakatsuji, N. Kiyohara, and T. Higo, Large anomalous Hall effect in a non-collinear antiferromagnet at room temperature, Nature (London) **527**, 212 (2015).

[3] T. Chen, T. Tomita, S. Minami, M. Fu, T. Koretsune, M. Kitatani, I. Muhammad, D. Nishio-Hamane, R. Ishii, F. Ishii *et al.*, Anomalous transport due to Weyl fermions in the chiral antiferromagnets Mn_3X, X = Sn, Ge, Nat. Commun. **12**, 572 (2021).

[4] D. Hong, N. Anand, C. Liu, H. Liu, I. Arslan, J. E. Pearson, A. Bhattacharya, and J. S. Jiang, Large anomalous Nernst and inverse spin-Hall effects in epitaxial thin films of kagome semimetal Mn_3Ge, Phys. Rev. Mater. **4**, 094201 (2020).

[5] T. Higo and S. Nakatsuji, Thin film properties of the non-collinear Weyl antiferromagnet Mn_3Sn, J. Magn. Magn. Mater. **564**, 170176 (2022).

[6] X. Wang, H. Yan, X. Zhou, H. Chen, Z. Feng, P. Qin, Z. Meng, L. Liu, and Z. Liu, Noncollinear Mn_3Sn for antiferromagnetic spintronics, Mater. Today Phys. **28**, 100878 (2022).

[7] Y. Zhang, Y. Sun, H. Yang, J. Železný, S. P. P. Parkin, C. Felser, and B. Yan, Strong anisotropic anomalous Hall effect and spin Hall effect in the chiral antiferromagnetic compounds Mn_3X (X = Ge, Sn, Ga, Ir, Rh, and Pt), Phys. Rev. B **95**, 075128 (2017).

[8] Y. Takeuchi, Y. Yamane, J.-Y. Yoon, R. Itoh, B. Jinnai, S. Kanai, J. Ieda, S. Fukami, and H. Ohno, Chiral-spin rotation of non-collinear antiferromagnet by spin-orbit torque, Nat. Mater. **20**, 1364 (2021).

[9] K. Kondou, H. Chen, T. Tomita, M. Ikhlas, T. Higo, A. H. MacDonald, S. Nakatsuji, and Y. Otani, Giant field-like torque by the out-of-plane magnetic spin Hall effect in a topological antiferromagnet, Nat. Commun. **12**, 6491 (2021).

[10] L. Zhu, D. C. Ralph, and R. A. Buhrman, Spin-orbit torques in heavy-metal–ferromagnet bilayers with varying strengths of interfacial spin-orbit coupling, Phys. Rev. Lett. **122**, 077201 (2019).

[11] P. J. Brown, V. Nunez, F. Tasset, J. B. Forsyth, and P. Radhakrishna, Determination of the magnetic structure of Mn_3Sn using generalized neutron polarization analysis, J. Phys. Condens. Matter **2**, 9409 (1990).

[12] N. H. Sung, F. Ronning, J. D. Thompson, and E. D. Bauer, Magnetic phase dependence of the anomalous Hall effect in Mn_3Sn single crystals, Appl. Phys. Lett. **112**, 132406 (2018).

[13] A. Markou, J. M. Taylor, A. Kalache, P. Werner, S. S. P. Parkin, and C. Felser, Noncollinear antiferromagnetic Mn_3Sn films, Phys. Rev. Mater. **2**, 051001(R) (2018).

[14] J. M. Taylor, A. Markou, E. Lesne, P. K. Sivakumar, C. Luo, F. Radu, P. Werner, C. Felser, and S. S. P. Parkin, Anomalous and topological Hall effects in epitaxial thin films of the non-collinear antiferromagnet Mn_3Sn, Phys. Rev. B **101**, 094404 (2020).

[15] T. Ikeda, M. Tsunoda, M. Oogane, S. Oh, T. Morita, and Y. Ando, Fabrication and evaluation of highly c-plane oriented Mn_3Sn thin films, AIP Adv. **10**, 15310 (2020).

[16] J. Yoon, Y. Takeuchi, R. Itoh, S. Kanai, S. Fukami, and H. Ohno, Crystal orientation and anomalous Hall effect of sputter-deposited non-collinear antiferromagnetic Mn_3Sn thin films, Appl. Phys. Express **13**, 13001 (2019).

[17] J.-Y. Yoon, Y. Takeuchi, S. DuttaGupta, Y. Yamane, S. Kanai, J. Ieda, H. Ohno, and S. Fukami, Correlation of anomalous Hall effect with structural parameters and magnetic ordering in $Mn_{3+x}Sn_{1-x}$ thin films, AIP Adv. **11**, 65318 (2021).

[18] P. K. Rout, P. V. Prakash Madduri, S. K. Manna, and A. K. Nayak, Field-induced topological Hall effect in the noncoplanar triangular antiferromagnetic geometry of Mn_3Sn, Phys. Rev. B **99**, 094430 (2019).

[19] S. Hu, D.-F. Shao, H. Yang, C. Pan, Z. Fu, M. Tang, Y. Yang, W. Fan, S. Zhou, E. Y. Tsymbal et al., Efficient perpendicular magnetization switching by a magnetic spin Hall effect in a noncollinear antiferromagnet, Nat. Commun. **13**, 4447 (2022).

[20] N. Nagaosa and Y. Tokura, Topological properties and dynamics of magnetic skyrmions, Nat. Nanotechnol. **8**, 899 (2013).

[21] W. Jiang, G. Chen, K. Liu, J. Zang, S. G. E. te Velthuis, and A. Hoffmann, Skyrmions in magnetic multilayers, Phys. Rep. **704**, 1 (2017).

[22] T. Xu, Z. Chen, H.-A. Zhou, Z. Wang, Y. Dong, L. Aballe, M. Foerster, P. Gargiani, M. Valvidares, D. M. Bracher et al., Imaging the spin chirality of ferrimagnetic Néel skyrmions stabilized on topological antiferromagnetic Mn_3Sn, Phys. Rev. Mater. **5**, 084406 (2021).

[23] N. Romming, C. Hanneken, M. Menzel, J. E. Bickel, B. Wolter, K. von Bergmann, A. Kubetzka, and R. Wiesendanger, Writing and deleting single magnetic skyrmions, Science **341**, 636 (2013).

[24] T. Yokouchi, N. Kanazawa, A. Tsukazaki, Y. Kozuka, A. Kikkawa, Y. Taguchi, M. Kawasaki, M. Ichikawa, F. Kagawa, and Y. Tokura, Formation of in-plane skyrmions in epitaxial

MnSi thin films as revealed by planar Hall effect, J. Phys. Soc. Japan **84**, 104708 (2015).

[25] N. Kanazawa, S. Seki, and Y. Tokura, Noncentrosymmetric magnets hosting magnetic skyrmions, Adv. Mater. **29**, 1603227 (2017).

[26] M. Hirschberger, T. Nakajima, M. Kriener, T. Kurumaji, L. Spitz, S. Gao, A. Kikkawa, Y. Yamasaki, H. Sagayama, H. Nakao et al., High-field depinned phase and planar Hall effect in the skyrmion host Gd_2PdSi_3, Phys. Rev. B **101**, 220401(R) (2020).

[27] N. Mohanta, S. Okamoto, and E. Dagotto, Planar topological Hall effect from conical spin spirals, Phys. Rev. B **102**, 064430 (2020).

[28] H. Li, B. Ding, J. Chen, Z. Li, X. Xi, G. Wu, and W. Wang, Planar topological Hall effect in a hexagonal ferromagnetic Fe_5Sn_3 single crystal, Appl. Phys. Lett. **118**, 182407 (2021).

[29] X. Li, C. Collignon, L. Xu, H. Zuo, A. Cavanna, U. Gennser, D. Mailly, B. Fauqué, L. Balents, Z. Zhu et al., Chiral domain walls of Mn_3Sn and their memory, Nat. Commun. **10**, 3021 (2019).

[30] K. Momma and F. Izumi, VESTA3 for three-dimensional visualization of crystal, volumetric and morphology data, J. Appl. Crystallogr. **44**, 1272 (2011).

[31] Y. You, X. Chen, X. Zhou, Y. Gu, R. Zhang, F. Pan, and C. Song, Anomalous Hall effect-like behavior with in-plane magnetic field in noncollinear antiferromagnetic Mn_3Sn films, Adv. Electron. Mater. **5**, 1800818 (2019).

[32] See Supplemental Material at http://link.aps.org/supplemental/10.1103/PhysRevB.108.144435 for the surface topography of Mn_3Sn film using atomic force microscopy measurements and calculation of THE. It also contains Refs. [3,33].

[33] L. Šmejkal, A. H. MacDonald, J. Sinova, S. Nakatsuji, and T. Jungwirth, Anomalous Hall antiferromagnets, Nat. Rev. Mater. **7**, 482 (2022).

[34] T. Ikeda, M. Tsunoda, M. Oogane, S. Oh, T. Morita, and Y. Ando, Improvement of large anomalous Hall effect in poly-crystalline antiferromagnetic $Mn_{3+x}Sn$ thin films, IEEE Trans. Magn. **55**, 1 (2019).

[35] J. M. Taylor, E. Lesne, A. Markou, F. K. Dejene, P. K. Sivakumar, S. Pöllath, K. G. Rana, N. Kumar, C. Luo, H. Ryll et al., Magnetic and electrical transport signatures of uncompensated moments in epitaxial thin films of the non-collinear antiferromagnet Mn_3Ir, Appl. Phys. Lett. **115**, 62403 (2019).

[36] T. Nagamiya, S. Tomiyoshi, and Y. Yamaguchi, Triangular spin configuration and weak ferromagnetism of Mn_3Sn and Mn_3Ge, Solid State Commun. **42**, 385 (1982).

[37] X. Li, J. Koo, Z. Zhu, K. Behnia, and B. Yan, Field-linear anomalous Hall effect and Berry curvature induced by spin chirality in the kagome antiferromagnet Mn_3Sn, Nat. Commun. **14**, 1642 (2023).

[38] T. Ikeda, M. Tsunoda, M. Oogane, S. Oh, T. Morita, and Y. Ando, Anomalous Hall effect in polycrystalline Mn_3Sn thin films, Appl. Phys. Lett. **113**, 222405 (2018).

[39] R. C. Budhani, V. Sharma, E. Negusse, J. Casey, A. K. Pathak, J. T. Sadowski, and B. Kirby, Magnetotransport and magnetic textures in $Ho/FeCoGd/\beta$-W multilayers, Phys. Rev. B **105**, 024412 (2022).

[40] N. Nagaosa, J. Sinova, S. Onoda, A. H. MacDonald, and N. P. Ong, Anomalous Hall effect, Rev. Mod. Phys. **82**, 1539 (2010).

[41] H. Yang, Y. Sun, Y. Zhang, W.-J. Shi, S. S. P. Parkin, and B. Yan, Topological Weyl semimetals in the chiral antiferromagnetic materials Mn_3Ge and Mn_3Sn, New J. Phys. **19**, 15008 (2017).

[42] T. Li, L. Zhang, and X. Hong, Anisotropic magnetoresistance and planar Hall effect in correlated and topological materials, J. Vac. Sci. Technol. A **40**, 10807 (2022).

[43] T. McGuire and R. Potter, Anisotropic magnetoresistance in ferromagnetic 3*d* alloys, IEEE Trans. Magn. **11**, 1018 (1975).

[44] R. Nepal, V. Sharma, L. Pogue, N. Drichko, and R. C. Budhani, Disorder driven variations in magnetoresistance and planar Hall effect in Bi_2Te_3 thin films, Thin. Solid. Films **761**, 139520 (2022).

[45] J. Song, T. Oh, E. K. Ko, J. H. Lee, W. J. Kim, Y. Zhu, B.-J. Yang, Y. Li, and T. W. Noh, Higher harmonics in planar Hall effect induced by cluster magnetic multipoles, Nat. Commun. **13**, 6501 (2022).

[46] T. Higo, D. Qu, Y. Li, C. L. Chien, Y. Otani, and S. Nakatsuji, Anomalous Hall effect in thin films of the Weyl antiferromagnet Mn_3Sn, Appl. Phys. Lett. **113**, 202402 (2018).

[47] H. Sharma, A. Tulapurkar, and C. V. Tomy, Sign reversal of anisotropic magnetoresistance in $La_{0.7}Ca_{0.3}MnO_3/SrTiO_3$ ultrathin films, Appl. Phys. Lett. **105**, 222406 (2014).

[48] R. C. Budhani, J. S. Higgins, D. McAlmont, and J. Paglione, Planar Hall effect in *c*-axis textured films of $Bi_{85}Sb_{15}$ topological insulator, AIP Adv. **11**, 55020 (2021).

[49] S. Tomiyoshi, S. Abe, Y. Yamaguchi, H. Yamauchi, and H. Yamamoto, Triangular spin structure and weak ferromagnetism of Mn_3Sn at low temperature, J. Magn. Magn. Mater. **54–57**, 1001 (1986).

[50] A. Neubauer, C. Pfleiderer, B. Binz, A. Rosch, R. Ritz, P. G. Niklowitz, and P. Böni, Topological Hall effect in the *A* phase of MnSi, Phys. Rev. Lett. **102**, 186602 (2009).

[51] T. Kurumaji, T. Nakajima, M. Hirschberger, A. Kikkawa, Y. Yamasaki, H. Sagayama, H. Nakao, Y. Taguchi, T. Arima, and Y. Tokura, Skyrmion lattice with a giant topological Hall effect in a frustrated triangular-lattice magnet, Science **365**, 914 (2019).